Design and numerical analysis of a gold-coated photonic crystal fiber based refractive index sensor

Mohammad Rakibul Islam[1] · A. N. M. Iftekher[1] · Kazi Rakibul Hasan[1] ·
Md. Julkar Nayen[1] · Saimon Bin Islam[1] · Aadreeta Hossain[1] · Zareen Mustafa[1] ·
Tahia Tahsin[1]

Abstract

In the course of past decade, surface plasmon resonance (SPR) based photonic crystal fiber (PCF) sensors have shown phenomenal advancement. Many researchers have proposed a wider range of SPR-based sensors by this time. But many of these proposed sensors either show low sensitivity or it is very difficult to fabricate the sensors for real time applications. We present a simple circular shaped PCF SPR sensor which is easy to fabricate as well as shows high sensitivity in the visible and near-infrared spectroscopy. A chemically stable and inactive plasmonic material, gold is applied to the outer layer of the PCF structure to generate surface plasmon excitation. A perfectly matched layer is used to minimize radiation absorption towards the surface. The guiding properties and analytical evaluation are carried out using commercially available COMSOL Multiphysics version 5.4 on the basis of finite element method. In x-polarization mode, the maximal value of amplitude sensitivity and wavelength sensitivity (WS) of the proposed sensor is 1757.3RIU^{-1} (Refractive Index Unit) and 32,000 nm/RIU respectively. In addition to that, the proposed design exhibits high sensor resolution of 1.428×10^{-6} and figure of merit of 587.2 indicating a high-performance sensor and demonstrates birefringence of 0.004 RIU. Moreover, the proposed PCF-SPR sensor is composed of only six symmetrical circular air holes, which makes it fabrication friendly. Owing to the high performance of the proposed sensor and high fabrication probability makes the sensor a strong contender to be used in biomedical and biochemical applications.

✉ Mohammad Rakibul Islam
  rakibultowhid@yahoo.com

1 Electrical and Electronic Engineering, Islamic University of Technology, Board Bazar, Gazipur 1704, Bangladesh

1 Introduction

Biosensors are analytical devices that consolidate biological components with chemical detectors. Since last decades, biosensors based on surface plasmon resonance (SPR) have been comprehensively developed and implemented compared to other sensing technologies, for instance, PCF sensors (Islam et al. 2019; Rahman et al. 2020; Mou et al. 2020; Islam et al. 2019; Islam et al. 2017; 2018), fiber Bragg grating (FBG) sensors, photoluminescence, micro-ring resonator, resonant mirror (James and Tatam 2003; Sharma et al. 2007). On a metal–dielectric interface under total internal reflection state, a TM (transverse magnetic) or p-polarized incident light generates a longitudinal oscillation termed as surface plasmons. Surface plasmon resonance (SPR) is an optical event that occurs when frequency of the incident light corresponds to the oscillation of conduction electrons of a metal. SPR sensor provides a diverse array of applications in biological science, chemical science, gaseous phase, environment, and beyond as it offers instant detection capacity, more accuracy, real-time monitoring, and label-free detection (Hu and Ho 2017). Moreover, SPR sensors are economically efficient and easy to evaluate. SPR sensors are exceedingly sensitive to the slightest change in analyte refractive index (RI); therefore, it can detect an unknown substance by investigating the resonance peak shift in response.

Conventional SPR sensors are based on prism coupling since prism can actuate surface plasmons. Kretschmann configuration sensing technique is predicated on angular interrogation method, where impinging light is concentrated on metal through a lens (Knoll 1998). Even though prism-based sensors are cost-effective, they involve bulky and complicated machinery equipment. Hence, they are not compatible with remote sensing applications and curved surfaces (Bender and Dessy 1994). A particular form of optical fiber is used instead of a prism known as photonic crystal fiber (PCF), in which the cladding region contains periodic air-holes. The evanescent field traverses these air holes and strikes the metal surface. Consequently, on the metal–dielectric interface surface plasmon oscillations are generated. A significant advantage of the PCF SPR sensor is adaptability because the core-guided leaky-mode propagation along with the evanescent field can be restrained (Ahmmed et al. 2013; Aoni et al. 2013), and it is much smaller in size compared to prism-based sensors.

In SPR sensors, plasmonic materials are used as they exhibit negative real permittivity that eventually facilitates resonance. In general, gold (Au), silver (Ag), aluminum (Al), copper (Cu) are extensively utilized as plasmonic materials. Silver is extremely conductive material, has low material loss, and the resonance peak is more precise. But silver is unstable as it gets oxidized readily (Caucheteur et al. 2015); thus, it hampers the performance of the sensor (Naik et al. 2013). Copper is the second most conductive material. Although copper is cheaper than other materials, it has an oxidation problem that makes it impractical (Rifat 2016). Sometimes a thin bimetallic layer is added atop the silver layer to avert oxidation. On the contrary, gold shows more chemical stability than silver in any environment. Likewise, gold has a broader resonance peak, higher accuracy, and sensitivity (Rifat 2015). More recently titanium nitride (TiN) based SPR sensors have gained huge popularity because of the plasmonic material's high melting point and high chemical stability. Veerpal Kaur et al. proposed a TiN coated external sensing SPR PCF sensor for a RI range from 1.385 to 1.40 with amplitude sensitivity and wavelength sensitivity of 70 RIU^{-1} and 10,000 nm/RIU respectively (Kaur and Singh 2019). Yashar Esfahani Monfared proposed a SPR PCF sensor where TiN was used as the plasmonic material with an amplitude sensitivity of 206.25 RIU^{-1} and a wavelength sensitivity of 16,275 nm/RIU (Esfahani Monfared 2020). With the advance of research on PCF-SPR

sensors, numerous designs have been proposed with high wavelength sensitivity, high sensor resolution and ease of fabrication. Till now various types of PCFs have been explored by researchers including nano-wire based (Lu et al. 2014), internally glazed (Yang et al. 2017), D fashioned (Luan et al. 2015), and externally glazed (Min Liu et al. 2018). Internal sensing approach has been more common in case of research which has yielded a wide range of new PCF-SPR sensors. An internally glazed birefringent sensor with wide range analyte Refractive Index revealing was proposed by Liu et al. which exemplified maximum wavelength sensitivity of 6,300 nm/RIU (Liu 2018). An irregular SPR sensor for analyte RI detection was proposed where the maximum WS and sensor resolution attained was 22,000 nm/RIU and 4.54×10^{-6} RIU respectively (Al Mahfuz et al. 2019). A D-shaped PCF sensor exhibiting a sensitivity of 10,493 nm/RIU was proposed by Guowen et al. (An et al. 2017). In a more recent paper Yashar et al. proposed a D-shaped SPR sensor which exhibits very high wavelength sensitivity of 11,800 nm/RIU and an amplitude sensitivity of 820 RIU^{-1} (Monfared et al. 2021). Mahfuz et al. proposed a simple hexagonal lattice plasmonic biosensor with two ring air-holes with a maximum wavelength sensitivity of 12,000 nm/RIU and peak resolution of 8.33×10^{-6} RIU (Mahfuz et al. 2019). A dual-polarized sensitive PCF based SPR sensor is proposed with maximum wavelength sensitivity of 30,000 nm/RIU (Haider et al. 2019). Another internal sensing paper was suggested by Rifat et al. (Rifat et al. 2016). But internal sensing is not suitable. So, the research branched out to external sensing producing exemplary results. A graphene-coated fiber considering external sensing with a maximum wavelength sensitivity of 5000 nm/RIU was proposed by Dash and Jha (2014). A simple Au-TiO$_2$ based PCF-SPR sensor was proposed with wavelength sensitivity of 25,000 nm/RIU and ease of fabrication (Islam 2019). Another design comprising of an air hole in the center was proposed that showed wavelength sensitivity of 18,000 nm/RIU (Haider et al. 2018). Using external sensing technique with a wavelength sensitivity of 62,000 nm/RIU was put forward (Islam et al. 2018). Although these sensors are proposed, none of these are yet fabricated. The first fabricated PCF SPR sensor showed a wavelength sensitivity of 2000 nm/RIU for a RI range from 1.38 to 1.41 (Wang et al. 2009). In this sensor gold was used as the plasmonic material. Elizaveta Klantsataya et al. proposed and fabricated an exposed core microstructured optical fiber (ECF) which showed a sensitivity of 1800 nm/RIU (Klantsataya et al. 2015). Silver was the plasmonic material in this case. Wei Chang Wong et al. fabricated a gold coated SPR sensor with a highest sensitivity of 3692 nm/RIU (Wong 2013). Although a large number of PCF sensors are proposed, most of the sensors are very difficult to fabricate and for internal sensing method, deposition of the gold layer outside the air hole is challenging. To overcome these problems, D-shaped PCFs are proposed where metal coating problem is solved. But this type of PCFs requires accurate polishing. Sensors with external sensing solve all these problems. But to acquire proper light guiding and higher sensitivity elliptical air holes need to be used. That is why in recent times researchers are trying their best to introduce external sensors having circular air holes with high sensitivity. These types of sensors are also very easy to fabricate. In this paper, a form of single square lattice PCF with circular air holes and a thin gold layer is designed and numerically examined. By changing different geometrical parameters, maximum performance parameters are obtained.

2 Structural design and theoretical modelling

Here, Fig. 1 demonstrates a cross-sectional aspect of the suggested circular lattice SPR based sensor. Opposite air holes from both sides are eliminated to ensure a steady flow of the evanescent field. In order to secure the maximum metal excitation two additional air holes are used specifically on the x-axis. Diameter of the existing air holes from the square layer is denoted by $d_1 = 1.96$ μm and the diameter of the additional air holes is denoted by $d_2 = 0.6$ μm. Analyte encircling a fine narrow gold layer is placed outside the fiber and the thickness of the gold layer is denoted by $t_g = 35$ nm. Analyte serves as a sensing medium, and its thickness ($t_a = 0.82$ μm) is selected based on the convergence test. Fused silica composed of a non-crystalline silica glass is used to surround the material, and its refractive index varies with the varying wavelength. It can be proved by Sellmeier equation (Islam et al. 2020)

$$n^2(\lambda) = 1 + \frac{B_1\lambda^2}{\lambda^2 - C_1} - \frac{B_2\lambda^2}{\lambda^2 - C_2} - \frac{B_3\lambda^2}{\lambda^2 - C_3} \tag{1}$$

Here, n and λ (μm) cites refractive index and wavelength in vacuum of fused silica (SiO$_2$) respectively. Sellmeier coefficients are respectively $B_1 = 0.69616300$, $B_2 = 0.407942600$, $B_3 = 0.897479400$, $C_1 = 4.67914826 \times 10^{-3}$ μm^2, $C_2 = 1.35120631 \times 10^{-2}$ μm^2 and $C_3 = 97.9340025$ μm^2. The relative permittivity of gold can be certainly determined by the Lorenz-Drude model (Vial et al. 2005).

$$\varepsilon_{Au} = \varepsilon_\alpha - \frac{\omega_D^2}{\omega(\omega + j\gamma D)} - \frac{\Delta\varepsilon.\Omega_L^2}{(\omega^2 - \Omega_L^2) + j\Gamma_L\omega} \tag{2}$$

where ε_{Au} is expressed as permittivity of gold, ε_α is expressed as permittivity at high frequency and the value is 5.9673, angular frequency is denoted by $\omega = 2\pi c/\lambda$. Here, damping frequency is denoted by γ_D, the plasmon frequency is denoted by ω_D and rest of the
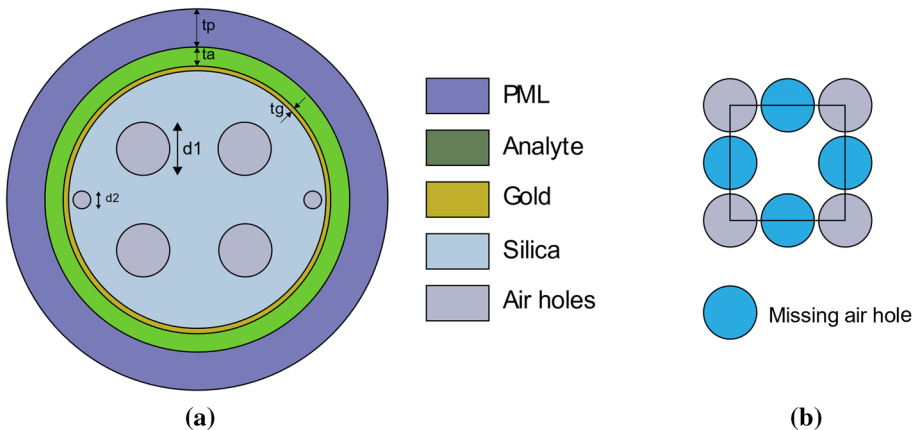

Fig. 1 **a** Cross-sectional aspect (2D) where $d_1 = 1.96$ μm, $d_2 = 0.6$ μm, $t_g = 35$ nm, $t_a = 0.82$ μm and $t_p = 1.2$ μm and **b** air-hole distribution of the suggested PCF SPR based biosensor

parameters of the equation are $\gamma_D/2\pi = 15.92$ THz, $\omega_D/2\pi = 2113.6$ THz, $\Omega_L = 650.07$ THz and the spectral width is denoted by $\Gamma_L/2\pi = 104.86$ THz.

PML (perfectly matched layer) having a width of 10% of the PCF structure and limiting conditions are applied to absorb the transitory field dispersed out of the PCF structure. The proposed sensor is designed and numerically investigated by available COMSOL Multiphysics 5.4 software using FEM (finite element method). The computational domain subdivided the structure into 23,120 triangle elements, 1752 edge elements with lowest quality of 0.5402, average quality of 0.8517, element area ratio of 0.01317, and mesh area of 156.3 μm².

PCF based sensors are developed based on coupling SPP (surface plasmon resonance) mode and primary core mode. Surface plasmon waves generated between metal-dielectric interfaces is the key aspect of this structure. At resonant wavelength, maximum energy transfers from the core mode to the SPP mode. Evanescent field of x-polarized and y-polarized mode diversifies with the geometry of the PCF fiber (Sazio et al. 2006). In this proposed sensor, we considered x-polarization as the fundamental mode due to its peak modal loss compared to y-polarization. Moreover, the evanescent field and excitation produced by y-polarization are lower than x-polarization.

Figure 2a, b demonstrates the arrangement of the core-guided form electric field and SPP form at analyte refractive index 1.39, respectively. Figure 2c expresses the scattered relation at Refractive index of 1.39 for x-polarization mode. Both practical refractive indices of core form and SPP form decrease when wavelength increases. At 800 nm wavelength, the core-guided form and the SPP form coincide. As the crossover point stage is perfectly matched, and maximum energy transformation transpires from core form to SPP form. Thereby at that particular point, confinement loss of core mode is found to be the highest. The modal loss is determined by the following calculation (Akowuah et al. 2012)

$$\alpha = 40\pi \cdot \text{Im}(n_{eff})/(ln(10)\lambda) \approx 8.686 \times k_0 \cdot \text{Im}[n_{eff}] \times 10^4 \text{ dB/cm} \tag{3}$$

where, $k_0 = 2\pi/\lambda$ is the wavenumber in the void.

Sensitivity can be deployed as a means of measurement of the conduct of any sensor which is PCF-based. Apart from a sensorgram curve being a suitable means for computing the susceptivity of a sensor, we propose using the amplitude and wavelength interrogation method for the detection of the sensitivity of the sensor. Nonetheless, the wavelength interrogation method is spectral-based, which utilizes the change in resonant wavelength to determine the value of analyte whereas, the amplitude interrogation technique is intensity-based, which utilizes the difference in the modal loss for the determination of the analyte. However, the use of a power meter and the unnecessary use of wavelength interpolation results in the amplitude interrogation method being comparatively less complicated, simple, and cost-effective at the same time. Amplitude susceptivity can be determined while using the following calculation (Li et al. 2019):

$$S_A(\lambda)[RIU^{-1}] = -\frac{1}{\alpha(\lambda, n_a)} \frac{\partial \alpha(\lambda, n_a)}{\partial n_a} \tag{4}$$

Here, $\alpha(\lambda, n_a)$ implies confinement loss at analyte RI, n_a, $\partial\alpha(\lambda, n_a)$ implies the confinement loss dissimilarity between two successive analyte refractive indexes in a row. In fact, amplitude interrogation technique is quite exposed to disturbances, which makes wavelength technique comparatively more responsive towards sensitivity. Sensitivity is obtained in the wavelength interrogation method using the following equation (Nooke et al. 2010)
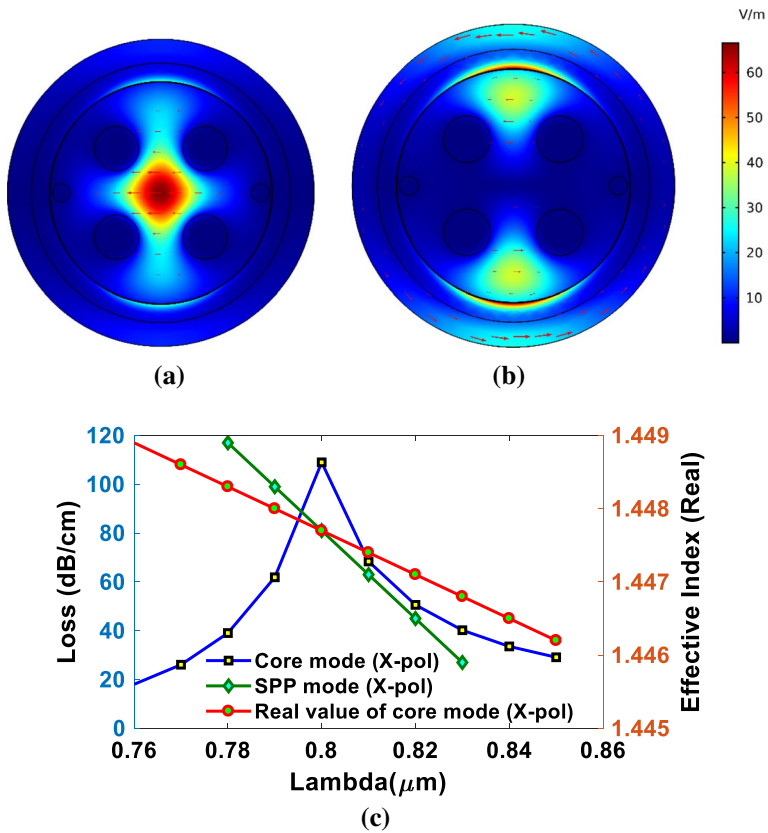
Fig. 2 **a** Core-guided form and **b** SPP form for x-polarization; **c** scattered relation between primary core-guided form and SPP form

$$S_\lambda(\lambda)[nm/RIU] = \Delta\lambda_{peak}/\Delta n_a \tag{5}$$

Here, $\Delta\lambda_{peak}$ is clearly the change in peak wavelength, Δn_a denoting the shift in two successive RI. Sensor Resolution plays a very significant role in disclosing the analyte RI variation. However, this sensor determination of a surface plasmon resonance is enhanced as the linewidth of the SPR indicating dip reduces, and the variation in the resonance shift increases. Sensor resolution is determined by the following calculation (Mahfuz et al. 2019):

$$R(RIU) = n_a \times \Delta\lambda_{min}/\Delta\lambda_{peak} \tag{6}$$

where λ_{min} is the least wavelength resolution. Besides the sensitivity as well as sensor resolution of a PCF- based sensor, Sensor length is an important parameter as well. The target goal of this paper is to present a design that allows its required transferred signal to maintain its undeviating polarization alongside the sensor length. Sensor length is specified by the following calculation (Otupiri et al. 2014):

$$L = \frac{1}{\alpha(\lambda, n_a)}. \tag{7}$$

3 Performance analysis of the proposed sensor

All geometrical parameters have a substantial impact over the performance of sensing. The phase-complementing points are assorted by altering parameters like thickness of gold (Au) layer, sensing layer, PML thickness, and pitch.

　Gold thickness plays a significant role in shifting the resonance wavelength resulting in affecting the performance evaluation of the sensor. An increment in gold thickness results in shifting the resonance wavelength to longer wavelengths. Maintaining a suitable range of lambda from 650 to 820 nm, we note that amplitude sensitivity increases progressively with an increase of gold thickness from 30 to 35 nm. Sensitivity reduces for 30 nm gold thickness because of the limitation called skin depth of surface plasmons (An et al. 2017). However, sensitivity ceases to decrease with further increment in Au thickness from 35 to 40 nm as it becomes very difficult for evanescent field to penetrate the gold layer and interplay the sensing layer (Haider et al. 2018), and thus, sensitivity peak 780.7 RIU^{-1} is obtained when the gold thickness is 35 nm. Thus, we optimize the layer at this point. Table 1 displays amplitude sensitivity variation with the alteration of gold thickness. Figure 3a, b illustrates the attaining of variation in gold thickness in x-polarization mode on the sensing performance.

　Figure 4a, b reflects the effect on sensitivity due to variance in the sensing layer, although the change is not that noteworthy. Keeping gold thickness 35 nm, the sensing layer has been changed and maximum sensitivity 881.2 RIU^{-1} is obtained for 0.82 μm. Table 2 displays performance comparison for different sensing layer lengths. The peak loss increases with the increasing value of analyte (Haider et al. 2018). Unfortunately, an increase in peak loss limits the value of sensitivity (Mahfuz et al. 2019). Initially, the sensitivity increased for an increase of analyte from 0.81 to 0.82 μm. However, with the increasing value of analyte from 0.82 to 0.85 μm the peak loss increases simultaneously resulting in the drop of sensitivity. Thus, maximum amplitude sensitivity is obtained for 0.82 μm.

　The flawlessly suited layer is used to assimilate radiation towards the surface. Although the thickness of PML does not affect much on the sensitivity of the sensor, but the thickness should be such that it can absorb the radiation successfully. Figure 5a, b shows confinement

Table 1 Amplitude sensitivity variation with the alteration of gold thickness

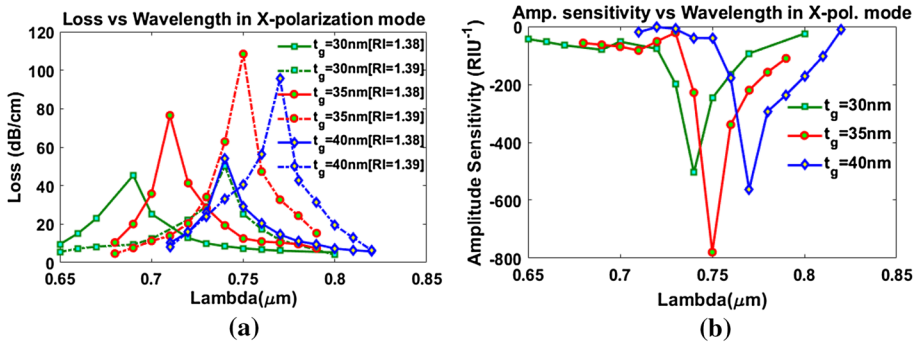| Gold (nm)	Analyte RI	Peak loss (dB/cm)	Wavelength sensitivity (nm/RIU)	Amplitude sensitivity (RIU^{-1})
30	1.38	45.28	4000	504.57
	1.39	50.15		
35	1.38	76.59	5000	780.07
	1.39	108.58		
40	1.38	54.28	3000	563.35
	1.39	95.62		

Fig. 3 Variation in confinement loss and amplitude sensitivity due to change in gold thickness at analyte refractive index $\eta_a = 1.38$ and 1.39
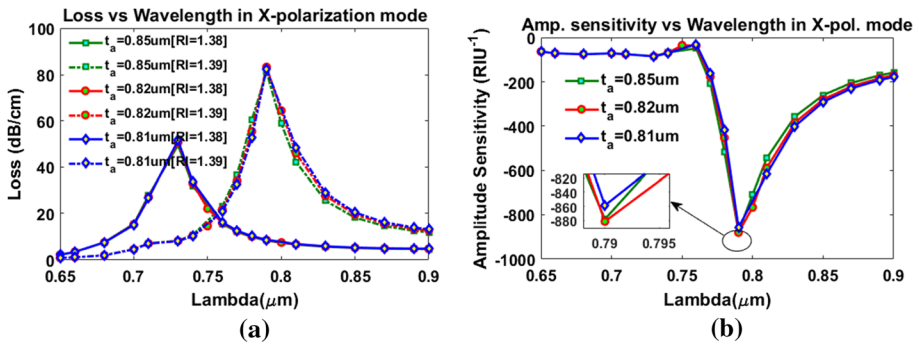

Fig. 4 Variation in confinement loss and amplitude sensitivity due to change in analyte thickness (sensing length) at analyte refractive index $\eta_a = 1.38$ and 1.39

Table 2 Amplitude sensitivity variation with the alternation of analyte layer

Analyte (μm)	Analyte RI	Peak loss (dB/cm)	Wavelength sensitivity (nm/RIU)	Amplitude sensitivity (RIU^{-1})
0.81	1.38	51.5	6000	858.5
	1.39	52.6		
0.82	1.38	50.7	6000	881.2
	1.39	55.42		
0.85	1.38	49.5	6000	877.89
	1.39	60.36		

loss and sensitivity of the offered sensor for different perfectly matched layer (PML) depth. Keeping gold thickness 35 nm and sensing length 0.82 μm, we changed PML thickness and acquired the following variation in peak loss and sensitivity in Table 3.

Even though the confinement loss is quite similar, we obtained improved sensitivity of 1032.9 RIU^{-1} for PML depth of 1.20 μm.
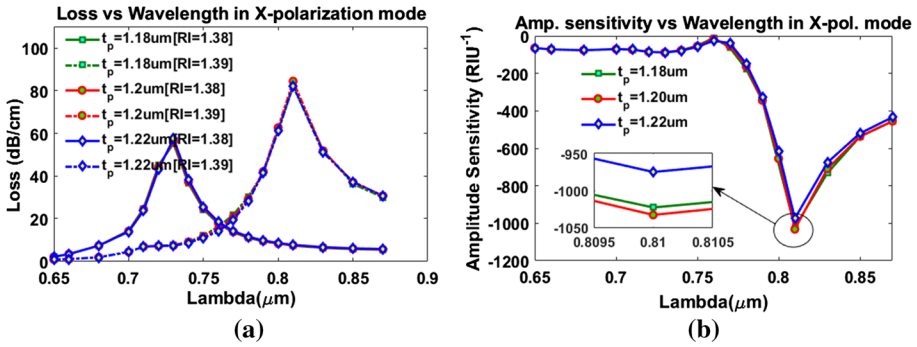
Fig. 5 Variation in confinement loss and amplitude sensitivity due to change in PML depth at analyte refractive index $\eta_a = 1.38$ and 1.39

Table 3 Amplitude sensitivity variation with the alteration of PML layer thickness

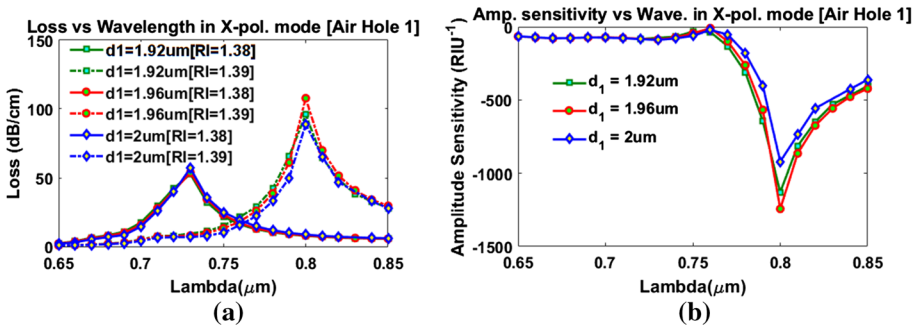| PML depth (μm)	Analyte RI	Peak loss (dB/cm)	Wavelength sensitivity (nm/RIU)	Amplitude sensitivity (RIU^{-1})
1.18	1.38	55.22	8000	1022.9
	1.39	82.01		
1.20	1.38	56.25	8000	1032.9
	1.39	84.51		
1.22	1.38	57.54	8000	975.3
	1.39	82.375		

Fig. 6 Variation in confinement loss and amplitude sensitivity due to change in diameter of center/large air holes at analyte refractive index $\eta_a = 1.38$ and 1.39

To increase sensor performance further the diameter of cladding air holes is varied. Figure 6a, b shows the change in confinement loss and in sensitivity due to change in center/large air holes. A peak sensitivity of 1244.1 RIU^{-1} is obtained for a diameter of 1.96 μm. When diameter is changed from 1.96 to 1.92 μm, the distance between center four air holes increases and thus evanescent field spreads over the channel between air holes. This

Table 4 Amplitude sensitivity variation with the alteration of diameter of center/large air holes

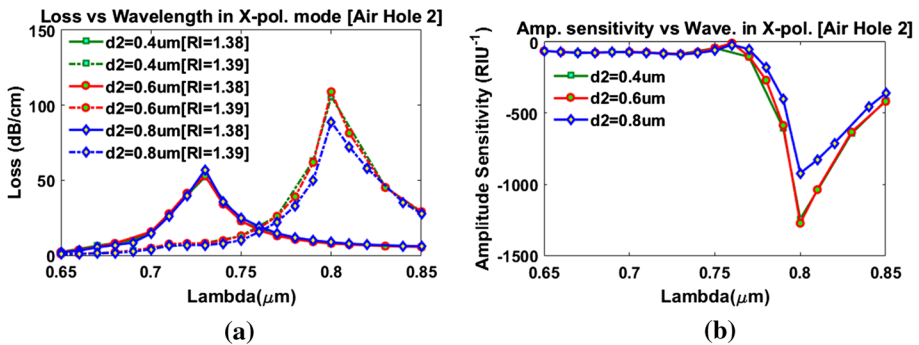| Diameter of cladding air hole (μm)	Analyte RI	Peak loss (dB/cm)	Wavelength sensitivity (nm/RIU)	Amplitude sensitivity (RIU^{-1})
1.92	1.38	52.69	7000	1129.3
	1.39	95.73		
1.96	1.38	53.71	7000	1244.1
	1.39	107.70		
2	1.38	57.01	7000	922.26
	1.39	88.81		

Fig. 7 Variation in confinement loss and amplitude sensitivity due to change in diameter of extra/small air holes at analyte refractive index $\eta_a = 1.38$ and 1.39

causes less excitation of surface plasmons and in return amplitude sensitivity decreases (Rifat et al. 2016). But when diameter is increased to 2 μm, the distance between center air holes decreases, making less guiding light towards the metal–dielectric interface and more towards the core and therefore amplitude sensitivity decreases for 2 μm diameter (Haider et al. 2018). Table 4 shows the variation in different parameters:

Effective excitation of the surface the metal is the core driver to the plasmonic phenomenon. At a particular wavelength, the incident light generates surface plasmon resonance. In this suggested design, initially, the diameter of the extra two air holes is kept 0.6 μm. Diameters smaller than this will cause a reduction in surface excitation, which is not acceptable. However, if the diameter is increased, the core-guided effective index will reduce along with the surface excitation (Rifat et al. 2016). Figure 7a, b is displaying the result on sensitivity due to variation in the extra air holes diameter in the cladding region.

From Table 5, utmost amplitude sensitivity of 1273.5 RIU^{-1} and wavelength sensitivity of 7000 nm/RIU is achieved considering a diameter of 0.6 μm.

Investigation of the proposed sensor is done by measuring confinement loss characteristics of various analytes. From Fig. 8a, we can observe that resonance peak retracts approaching longer wavelengths as analyte RI is increased. Besides, it changes RI of plasmonic mode that eventually alters the phase-matching points. The span of analyte RI is taken from 1.33 to 1.40, considering practical biochemical interactions. Figure 8b demonstrates the sensitivity of the proposed sensor, which is increasing with the increment of the

Table 5 Amplitude sensitivity variation with the alteration of diameter of extra/small two air holes

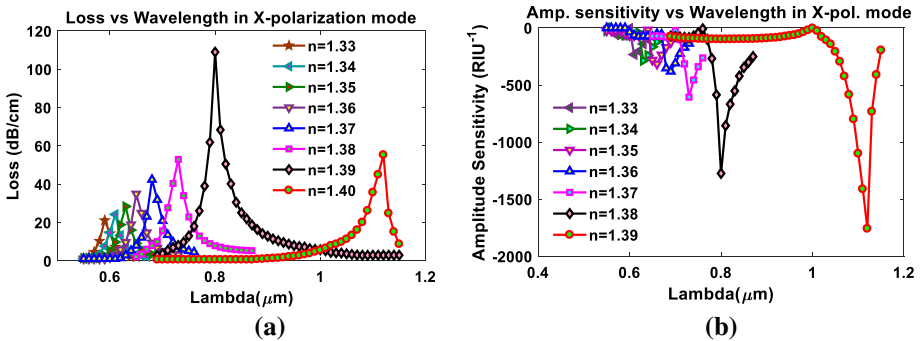| Diameter (µm)	Analyte RI	Peak loss (dB/cm)	Wavelength sensitivity (nm/RIU)	Amplitude sensitivity (RIU^{-1})
0.4	1.38	52.18	7000	1244.4
	1.39	63.04		
0.6	1.38	52.95	7000	1273.5
	1.39	61.90		
0.8	1.38	57.01	7000	922.26
	1.39	88.81		

Fig. 8 Variation in confinement loss and sensitivity due to change in analyte refractive index (1.33–1.39)

resonance peak. Table 6 shows the comparison of the characteristics of the proposed sensor for different RI of the analyte for x-polarization mode.

From the table, we can see greatest amplitude sensitivity and wavelength sensitivity is 1757.3 RIU^{-1} and 32,000 nm/RIU respectively. Also, we obtained a sensor resolution of 1.428×10^{-6} that implies the degree of detection for minimum change in lambda of 0.1 nm.

The figure of merit is the ratio between the sensitivity and the full width at half maximum (FWHM) for evaluating the performance of an SPR sensor, which can be described as follows: (Haider et al. 2019)

$$FOM = \frac{Sensitivity}{FWHM}(RIU^{-1}) \tag{8}$$

In general, FOM points out the quality performance of any device. For maintaining an overall higher sensing performance, it is required to maintain the figure of merit as high as possible. An expansion in sensitivity and reduction in FWHM simultaneously brings about the accretion of FOM. Again, for a plasmon sensor, the critical parameter of high FOM indicates high sensitivity and high wavelength resolution. Still, the figure of merit can be intensified by using a porous silica film with a lower refractive index (Meng et al. 2017). Performance improvement in the sensor validates the improvement of FOM. For the proposed design, maximum FOM obtained is 587.2.

Birefringence is a vital property of a PCF-SPR sensor as it increases the sensitivity and shows different sensitivity for x- and y-polarized mode signals. The input signal (linearly

Table 6 Performance analysis by altering analyte refractive index from 1.33 to 1.40

Analyte RI	Peak loss (dB/cm)	Res. peak wavelength (nm)	Res. peak shift(nm)	Amplitude sensitivity (RIU^{-1})	Wavelength sensitivity (nm/RIU)	Sensor resolution	FOM
1.33	21.14	590	20	233.56	2000	5×10^{-5}	189.2
1.34	24.28	610	20	286.62	2000	5×10^{-5}	164.7
1.35	28.43	630	20	315.778	2000	5×10^{-5}	140.7
1.36	34.99	650	20	380.93	3000	5×10^{-5}	207.0
1.37	42.42	680	30	605.84	5000	3.33×10^{-5}	235.7
1.38	52.95	730	50	1273.5	7000	2×10^{-5}	264.4
1.39	108.99	800	70	1757.3	32,000	1.428×10^{-6}	587.2
1.40	55.35	–	–	N/A	N/A	N/A	N/A

polarized light) launched on the x or y axis of the fiber preserves the polarization state throughout the fiber length which is independent of exterior mechanical and thermal agitations the fiber may suffer. In addition, a birefringent fiber is essential for signal reception when it is launched in one of the fiber polarization axes. By choosing the input signal in the y or x axes, selection between improving the fiber sensitivity in one axis and reducing the loss in other axis can be done (Islam 2019). Also, birefringence shows the coupling efficiency of a fiber. It can be calculated using: (Islam et al. 2018; Islam et al. 2020)

$$B = \left| n_x - n_y \right| \tag{9}$$

Here, n_x denotes the effective mode index (EMI) in the x-pol. and n_y denotes the EMI in y-pol. respectively. Generally, circular or solid core fibers show almost zero birefringence. For simplicity of fabrication and practical implementation, we use circular symmetrical air-holes thus we obtained birefringence of 0.0004 RIU, which is a promising trade-off between structural complexity and sensitivity.

Figure 9a shows the variation in sensor length compared to different analyte RI. Sensor length diminishes with the augmentation of the analyte refractive index as it completely depends on absorption loss. From the figure, we can say, the possibility of the use of sensing length of a few millimeters to centimeters to detect unidentified analytes is possible.

Assessment of sensors for particularly higher RI analytes requires high linear fitting characteristics (Otupiri et al. 2014). Generally, high linearity is desirable as it is an indication of a high-quality sensor. In this case, the linear fit is an essential parameter necessary for the optimization of the sensor. To avoid the complexity of the detection process, the non-linear fitting characteristic is not preferable. However, the slope of the linear fitting curve usually points out the mean sensitivity of a PCF- based sensor, which is somewhat disrupted by the non-linear fitting property (Hasan et al. 2018). Figure 9b illustrates that the proposed sensor shows a linearly fitted curve with a R^2 value of 0.998. The linear regression line equation is $y = 2x - 2.07$, where, x, y denotes the refractive index of the analyte, resonance wavelength, respectively.

The fabrication tolerance for the design has been investigated as given in the Fig. 10. As during fabrication, the exact measurements for the parameters are impossible to maintain so we have considered $\pm 10\%$ variation from the optimized value in the parameters to see if the fabrication is still acceptable with such variations. The gold thickness is optimized at
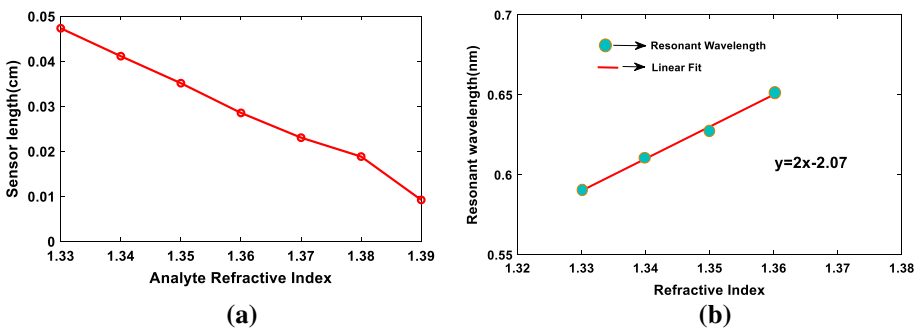

Fig. 9 **a** Change in sensor length with increment of analyte RI; **b** regression line for resonance wavelength variation with analyte Refractive Index
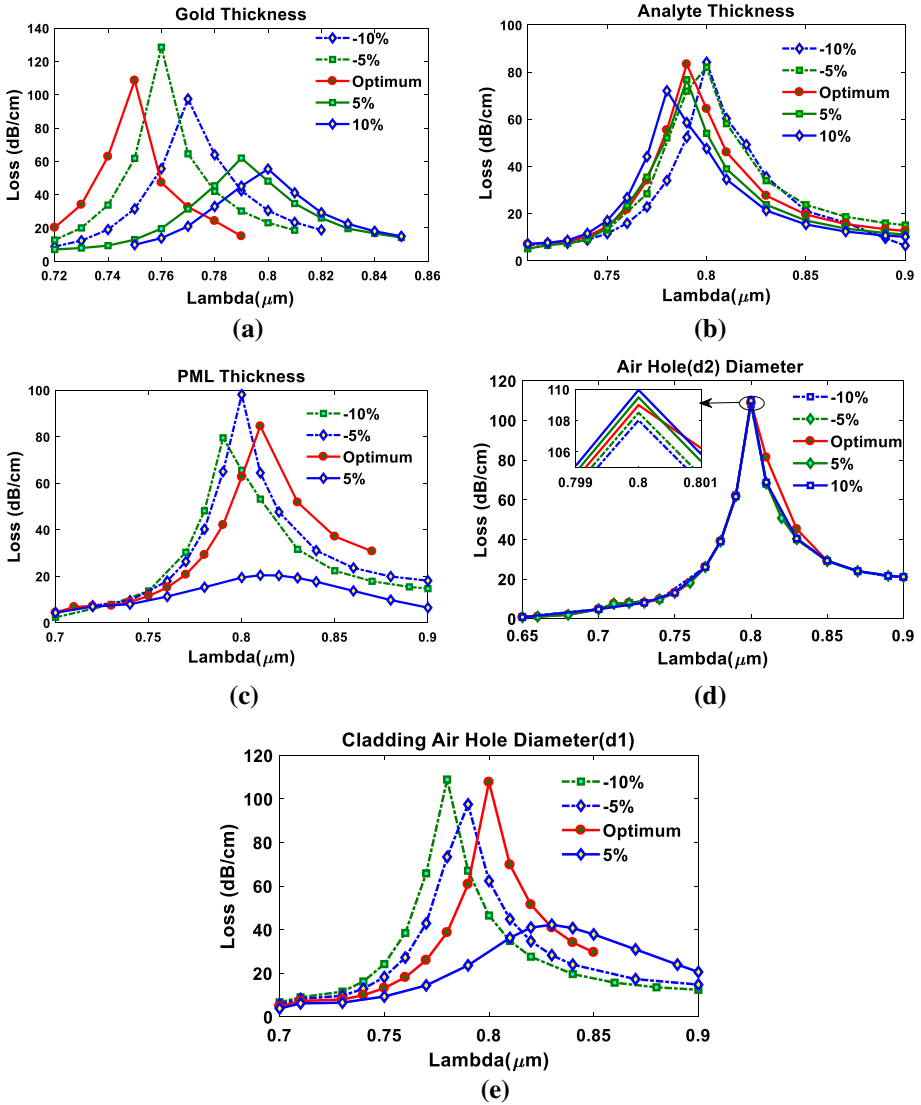
Fig. 10 Loss spectrums for variation in **a** gold layer thickness, **b** analyte thickness, **c** PML thickness, **d** diameter of cladding air hole, and **e** diameter of small air hole for x-polarized mode

35 nm which is shown in Fig. 10a. Gold layer thickness exhibits huge impact on sensitivity and loss depth (Liu et al. 2018). A thin gold layer shows higher loss depth and sensitivity (Chen et al. 2018). Due to ± 10% variation in the gold layer thickness, the variation observed in loss depth and sensitivity is negligible compared to that of the optimum value.

The analyte has been optimized at 0.82 μm and considering the variations, the resonant wavelength remains within ± 2% of the optimized value which has been shown in Fig. 10b. Though, loss depth is changed moderately yet the resonant wavelength variation is negligible where we concluded to keep the analyte optimized value at 0.82 μm.

In the case of PML shown in Fig. 10c, the optimized value obtained is at 1.2 μm and for the variations, the resonant wavelength remains within ± 5% of the optimized value. The mirroring of the light-penetration from PCF is absorbed depending on the PML thickness (Haider et al. 2019). PML thickness difference of 10% marginally altered imaginary part of Effective-Index (EI) which results in small variation in loss depth. However, the resonant wavelength variation remains negligible which exhibits unaltered sensor performance.

The diameter of the smaller circles (d_2) has significant dominance over the sensing execution by signifying phase-matching phenomena. The smaller hole diameters have been optimized at $d_2 = 0.6$ μm; if it is decreased gradually, the EI of core guided mode becomes low. As a result, controlling light seems to disseminate towards cladding region, which results in higher confinement loss and prevents the practical realization. On the other hand, if the value is increased, the light will be more gathered towards the core however surface excitation is given more priority for SPR (Haider et al. 2018). The variations of d_2 show contrast in loss depth. The increment in d_2 conveys decrease in loss depth while decreasing it shows drastic reduction of loss depth. The resonant wavelength of the variations remains within ± 3% of the optimized value for d_2 shown in Fig. 10d.

Considering the cladding air holes, the optimization is seen at $d_1 = 1.96$ μm shown in Fig. 10e. The variation in d_1 exhibits an opposite effect on the sensing compared to d_1 (Haider et al. 2018). However, the loss for variation is negligible but the resonant wavelength shifts a bit. Increasing diameter of larger air holes by 5%, decreases the loss spectrum. As the resonant wavelength remains in a close range, so it does not seem to have effect over fabrication. From investigating the fabrication tolerance, it is noticed that while varying the parameters ± 10%, there is change in the loss depth, the resonant wavelength remains fairly the same. So, sensing performance will not be hampered after fabrication. Since the structure is simple, the offered PCF can be fabricated by the standard Stack-and-Draw fiber drawing method (Mahdiraji et al. 2014). The thin gold layer is placed by Chemical Vapor Deposition and sputtering techniques as they are the most common methods to coat PCF structures (Yu et al. 2009). Also considering recent advancement, Atomic Layer Deposition (ALD) can be used for gold-layer coating (Rifat et al. 2019).

4 Conclusion

A simple single-layer square lattice plasmonic PCF biosensor is proposed here with external sensing operability. The objective of this research is to put forward draft based wholly on annular air holes. We have considered all structural parameters to attain the maximum sensitivity and sensor resolution possible. Table 7 depicts the performance analysis comparison between the proposed biosensor and previously reported sensors. The proposed sensor offers highest amplitude sensitivity of 1757.3 RIU^{-1} and highest wavelength sensitivity of 32,000 nm/RIU. Sensor resolution of 1.428×10^{-6}, FOM of 587.2, and birefringence of 0.004 RIU is obtained for x-polarization, which means it can ascertain very little alteration in the analyte. Moreover, small sensor length is required, and fabrication can also be done using the usual Stack and Draw method. Moreover, using CVD (chemical vapor deposition) method plasmonic gold layer can be placed on the structure to alleviate fabrication and making it practically manufacturable. Due to improved modal properties with a simple structure, this proposed sensor can be implemented in numerous real-time diagnostic studies in biomedical, biochemical applications.

Table 7 Performance comparison between proposed sensors and prior stated sensors

Refs.	RI range	Max. amplitude sensitivity (RIU^{-1})	Max. wavelength ensitivity (nm/RIU)	Sensor resolution	FOM	Birefringence
Otupiri et a (2014)	1.46–1.485	820	23,000	4.35×10^{-6}	–	–
Hasan et al. (2018)	1.33–1.37	860	5000	4×10^{-5}	–	–
Liu et al. (2018)	1.18–1.36	1054	20,000	5×10^{-6}	250	–
Chen et al. (2018)	1.33–1.43	1086	44,000	2.2×10^{-6}	502	1.6×10^{-3}
Mahfuz et al. (2019)	1.36–1.41	1222	14,660	6.82×10^{-6}	1140	1.2×10^{-3}
Mahdiraji et al. (2014)	1.33–1.38	1411	25,000	4×10^{-6}	–	–
Yu et al. (2009)	1.33–1.43	1415	6200	1.61×10^{-6}	–	–
Rifat et al. (2019)	1.33–1.39	1506	22,000	6.64×10^{-6}	508	–
This paper	1.33–1.39	1757.3	32,000	1.428×10^{-6}	587.2	4×10^{-4}

Compliance with ethical standards

Conflict of interest The authors declares no conflicts of interest.

References

Ahmmed, R., Ahmed, R., Razzak, S.M.A.: Design of large negative dispersion and modal analysis for hexagonal, square, FCC and BCC photonic crystal fibers. In: 2013 International Conference on Informatics, Electronics and Vision (ICIEV), Dhaka, pp. 1–6 (2013)

Akowuah, E.K., Gorman, T., Ademgil, H., Haxha, S., Robinson, G.K., Oliver, J.V.: Numerical analysis of a photonic crystal fiber for biosensing applications. IEEE J. Quantum Electron. **48**(11), 1403–1410 (2012)

Al Mahfuz, M., Hasan, M.R., Momota, M.R., Masud, A., Akter, S.: Asymmetrical photonic crystal fiber based plasmonic sensor using the lower birefringence peak method. OSA Continuum **2**, 1713–1725 (2019)

An, G., Hao, X., Li, S., Yan, X., Zhang, X.: D-shaped photonic crystal fiber refractive index sensor based on surface plasmon resonance. Appl. Opt. **56**, 6988–6992 (2017)

Aoni, R.A., Ahmed, R., Abdur Razzak, S.M.: Design and simulation of duel-concentric-core photonic crystal fiber for dispersion compensation. In Rolland, J., Wyant, J., Chavel, P., Zhang, X., Wang, C., Bai, Y., (eds.), 2013 CIOMP-OSA Summer Session on Optical Engineering, Design and Manufacturing, Optical Society of America, paper Tu2 (2013)

Bender, W.J., Dessy, R.E.: Surface plasmon resonance sensor. Google Patents (1994)

Caucheteur, C., Guo, T., Albert, J.: Review of plasmonicfiber optic biochemical sensors: improving the limit of detection. Anal. Bioanal. Chem. **407**, 3883–3897 (2015)

Chen, X., Xia, Li., Chen, Li.: Surface plasmon resonance sensor based on a novel d shaped photonic crystal fiber for low refractive index detection. IEEE Photon. J. **10**(1), 1–9 (2018)

Dash, J.N., Jha, R.: Graphene-based birefringent photonic crystal fiber sensor using surface plasmon resonance. IEEE Photon. Technol. Lett. **26**(11), 1092–1095 (2014)

EsfahaniMonfared, Y.: Refractive index sensor based on surface plasmon resonance excitation in a D-shaped photonic crystal fiber coated by titanium nitride. Plasmonics **15**, 535–542 (2020)

Haider, F., Aoni, R.A., Ahmed, R., Miroshnichenko, A.E.: Highly amplitude-sensitive photonic-crystal-fiber-based plasmonic sensor. J. Opt. Soc. Am. B **35**, 2816–2821 (2018)

Haider, F., Aoni, R.A., Ahmed, R., Islam, M.S., Miroshnichenko, A.E.: Propagation controlled photonic crystal fiber-based plasmonic sensor via scaled-down approach. IEEE Sens. J. **19**(3), 962–969 (2019)

Hasan, M.R., Akter, S., Rifat, A.A., SRana, K Ahmed, R Ahmed, H Subbaraman, D Abbott, : Spiral photonic crystal fiber-based dual-polarized surface plasmon resonance biosensor. IEEE Sens. J. **18**(1), 133–140 (2018)

Hu, D.J.J., Ho, H.P.: Recent advances in plasmonic photonic crystal fibers: design, fabrication and applications. Adv Opt. Photon. **9**, 257–314 (2017)

Islam, M.S., Sultana, J., Dinovitser, A., Ahmed, K., Islam, M.R., Faisal, M., Ng, W.-H. , Abbott, D.: A novel zeonex based photonic sensor for alcohol detection in beverages. In: IEEE International Conference on Telecommunications and Photonics (ICTP), pp. 114–118 (2017)

Islam, M.S., Sultana, J., Rifat, A.A., Ahmed, R., Dinovitser, A., Ng, B.W.-H., Ebendorff-Heidepriem, H., Abbott, D.: Dual-polarized highly sensitive plasmonic sensor in the visible to near-IR spectrum. Opt. Express **26**, 30347–30361 (2018)

Islam, M.S., Sultana, J., Ahmed, K., Islam, M.R., Dinovitser, A., Ng, B.W.H., Abbott, D.: Terahertz detection of alcohol using a photonic crystal fiber sensor. Appl. Opt. **57**(10), 2426–33 (2018)

Islam, M.S., Sultana, J., Ahmed, K., Dinovitser, A., Islam, M.R., Ng, B.W.-H., Abbott, D.: A novel approach for spectroscopic chemical identification using photonic crystal fiber in the terahertz regime. IEEE Sens. J. **18**(2), 575–582 (2018)

Islam, M.S., et al.: A Hi-Bi ultra-sensitive surface plasmon resonance fiber sensor. IEEE Access **7**, 79085–79094 (2019)

Islam, M.R., Kabir, M.F., Talha, K.M.A., Islam, M.S.: A novel hollow core terahertz refractometric sensor. Sens. BioSens. Res. **25**, 100295 (2019)

Islam, M.S., Islam, M.R., Sultana, J., Dinovitser, A., Ng, B.W.H., Abbott, D.: Exposed core localized surface plasmon resonance biosensor. J. Opt. Soc. Am. B **36**(8), 2306–2311 (2019)

Islam, M.R., Iftekher, A.N.M., Hasan, K.R., Nayen, M.J., Islam, S.B.: Dual-polarized highly sensitive surface-plasmon-resonance-based chemical and biomolecular sensor. Appl. Opt. **59**, 3296–3305 (2020)

Islam, M.A., Islam, M.R., Islam Khan, M.M., Chowdhury, J.A., Mehjabin, F., Islam, M.: Highly birefringent slotted core photonic crystal fiber for THz wave propagation. Phys. Wave Phen. **28**(1), 58–67 (2020)

James, S.W., Tatam, R.P.: Optical fibre long-period grating sensors: characteristics and application. Meas. Sci. Technol. **14**, R49 (2003)

Kaur, V., Singh, S.: Design of titanium nitride coated PCF-SPR sensor for liquid sensing applications. Opt. Fiber Technol. **48**, 159–164 (2019)

Klantsataya, E., François, A., Ebendorff-Heidepriem, H., Hoffmann, P., Monro, T.: Surface plasmon scattering in exposed core optical fiber for enhanced resolution refractive index sensing. Sensors **15**(10), 25090–25102 (2015)

Knoll, W.: Interfaces and thin films as seen by bound electromagnetic waves. Annu. Rev. Phys. Chem. **49**(1), 569–638 (1998)

Li, Z., Yu, Z., Shen, Y., Ruan, X., Dai, Y.: Graphene enhanced leaky mode resonance in tilted fiber Bragg grating: a new opportunity for highly sensitive fiber optic sensor. IEEE Access **7**, 26641–26651 (2019)

Liu, C., et al.: Birefringent PCF-based SPR sensor for a broad range of low refractive index detection. IEEE Photon. Technol. Lett. **30**(16), 1471–1474 (2018)

Liu, C., Su, W., Liu, Q., et al.: Symmetrical dual D-shape photonic crystal fibers for surface plasmon resonance sensing. Opt. Express **26**(7), 9039–9049 (2018)

Lu, Y., Wang, M.T., Hao, C.J., Zhao, Z.Q., Yao, J.Q.: Temperature sensing using photonic crystal fiber filled with silver nanowires and liquid. IEEE Photon. J. **6**(3), 1–7 (2014)

Luan, N., Wang, R., Lv, W., Yao, J.: Surface plasmon resonance sensor based on D-shaped microstructured optical fiber with hollow core. Opt. Express **23**, 8576–8582 (2015)

Mahdiraji, G.A., Chow, D.M., Sandoghchi, S.R., Amirkhan, F., Dermosesian, E., Yeo, K.S., Kakaei, Z., Ghomeishi, M., Poh, S.Y., Gang, S.Y., Adikan, F.R.M.: Challenges and solutions in fabrication of silica-based photonic crystal fibers: an experimental study. FiberIntegr. Opt. **33**, 1–2 (2014)

Mahfuz, M.A., Mollah, M.A., Momota, M.R., Paul, A.K., Masud, A., Akter, S., Hasan, M.R.: Highly sensitive photonic crystal fiber plasmonic biosensor: design and analysis. Opt. Mater. **90**, 315–321 (2019)

Mahfuz, M.A., Hossain, M.A., Haque, E., Hai, N.H., Namihira, Y., Ahmed, F.: A bimetallic-coated, low propagation loss, photonic crystal fiber based plasmonic refractive index sensor. Sensors **19**, 3794 (2019)

Meng, Q.-Q., Zhao, X., Lin, C.-Y., Chen, S.-J., Ding, Y.-C., Chen, Z.-Y.: Figure of merit enhancement of a surface plasmon resonance sensor using a low-refractive-index porous silica film. Sensors **17**, 1846 (2017)

Min Liu, Xu., Yang, P.S., Yuan, H.: High-sensitivity birefringent and single-layer coating photonic crystal fiber biosensor based on surface plasmon resonance. Appl. Opt. **57**, 1883–1886 (2018)

Monfared, Y.E., Hajati, M., Liang, C., Yang, S., Qasymeh, M.: Quasi-D-shaped fiber optic plasmonic biosensor for high-index analyte detection. IEEE Sens. J. **21**(1), 17–23 (2021)

Mou, F.A., Rahman, M.M., Islam, M.R., Bhuiyan, M.I.H.: Development of a photonic crystal fiber for THz wave guidance and environmental pollutants detection. Sens. Bio-Sens. Res. **29**, 100346 (2020)

Naik, G.V., Shalaev, V.M., Boltasseva, A.: Alternative plasmonic materials: beyond gold and silver. Adv. Mater. **25**(24), 3264–3294 (2013)

Nooke, A., Beck, U., Hertwig, A., Krause, A., Krüger, H., Lohse, V., Negendank, D., Steinbach, J.: On the application of gold based SPR sensors for the detection of hazardous gases. Sens. Actuat. B Chem. **149**(1), 194–198 (2010)

Otupiri, R., Akowuah, E.K., Haxha, S., Ademgil, H., AbdelMalek, F., Aggoun, A.: A novel birefrigent photonic crystal fiber surface plasmon resonance biosensor. IEEE Photon. J. **6**(4), 1–11 (2014)

Rahman, M.M., Mou, F.A., Bhuiyan, M.I.H., Islam, M.R.: Photonic crystal fiber based terahertz sensor for cholesterol detection in human blood and liquid foodstuffs. Sens. BioSens. Res. **29**, 100356 (2020)

Rifat, A.A., et al.: Surface plasmon resonance photonic crystal fiber biosensor: a practical sensing approach. IEEE Photon. Technol. Lett. **27**(15), 1628–1631 (2015)

Rifat, A.A., et al.: Copper-graphene-based photonic crystal fiberplasmonic biosensor. IEEE Photon. J. **8**(1), 1–8 (2016)

Rifat, A.A., AmouzadMahdiraji, G., Shee, Y.G., JubayerShawon, M., MahamdAdikan, F.R.: A novel photonic crystal fiber biosensor using surface plasmon resonance. Procedia Eng. **140**, 1–7 (2016)

Rifat, A.A., Rabiul Hasan, M., Ahmed, R., Miroshnichenko, A.E.: Microstructured optical fiber-based plasmonic sensors. In: Hameed, M., Obayya, S. (eds.) Computational Photonic Sensors. Springer, Cham (2019)

Sazio, J.A., Amezcua-Correa, A., Finlayson, C.E., Hayes, J.R., Scheidemantel, T.J., Baril, N.F., Jackson, B.R., Won, D.J., Zhang, F., Margine, E.R., Gopalan, V., Crespi, V.H., Badding, J.V.: Microstructured optical fibers as high-pressure microfluidic reactors. Science **311**(5767), 1583–1586 (2006)

Sharma, A.K., Jha, R., Gupta, B.D.: Fiber-optic sensors based on surface plasmon resonance: a comprehensive review. IEEE Sens. J. **7**(8), 1118–1129 (2007)

Vial, A., Grimault, A.-S., Macías, D., Barchiesi, D., de La Chapelle, M.L.: Improved analytical fit of gold dispersion: application to the modeling of extinction spectra with a finite-difference time-domain method. Phys. Rev. B **71**, 085416 (2005)

Wang, A., Docherty, A., Kuhlmey, B.T., Cox, F.M., Large, M.C.J.: Side-hole fiber sensor based on surface plasmon resonance. Opt. Lett. **34**, 3890–3892 (2009)

Wong, W.C., et al.: Photonic crystal fiber surface plasmon resonance biosensor based on protein G immobilization. IEEE J. Sel. Top. Quantum Electron. **19**(3), 4602107–4602107 (2013)

Yang, X., Lu, Y., Liu, B., et al.: Analysis of graphene-based photonic crystal fiber sensor using birefringence and surface plasmon resonance. Plasmonics **12**, 489–496 (2017)

Yu, X., Zhang, Y., Pan, S., Shum, P., Yan, M., Leviatan, Y., Li, C.: A selectively coated photonic crystal fiber-based surface plasmon resonance sensor. J. Opt. **12**, 015005 (2009)

Publisher's Note Springer Nature remains neutral with regard to jurisdictional claims in published maps and institutional affiliations.